Quantitative Photoacoustic Imaging of Nanoparticles in Cells and Tissues

Jason R. Cook, Wolfgang Frey, and Stanislav Emelianov*

Department of Biomedical Engineering, The University of Texas at Austin, 107 W. Dean Keeton, Stop C0800, Austin, Texas 78712, United States

ABSTRACT Quantitative visualization of nanoparticles in cells and tissues, while preserving the spatial information, is very challenging. A photoacoustic imaging technique to depict the presence and quantity of nanoparticles is presented. This technique is based on the dependence of the photoacoustic signal on both the nanoparticle quantity and the laser fluence. Quantitative photoacoustic imaging is a robust technique that does not require knowledge of the local fluence, but a relative change in the fluence. This eliminates the need for sophisticated methods or models to determine the energy distribution of light in turbid media. Quantitative photoacoustic imaging was first applied to nanoparticle-loaded cells, and quantitation was validated by inductively coupled plasma mass spectrometry. Quantitative photoacoustic imaging was then extended to xenograft tumor tissue sections, and excellent agreement with traditional histopathological analysis was demonstrated. Our results suggest that quantitative photoacoustic imaging may be used in many applications including the determination of the efficiency and effectiveness of molecular targeting strategies for cell studies and animal models, the quantitative assessment of photoacoustic contrast agent biodistribution, and the validation of *in vivo* photoacoustic imaging.

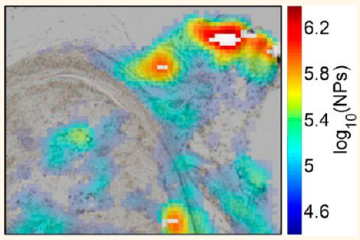

KEYWORDS: nanoparticle · quantitative photoacoustic imaging · photoacoustic microscopy · histology · molecular sensing · cancer

Molecular imaging promises to expand existing medical imaging techniques beyond the typical visualization of anatomical features to incorporate functional and pathological information based on contrast agents that include targeting capabilities.[1,2] Over the past decade, the biotechnological development of highly specific recognition elements and the nanotechnological development of contrast agents have opened strategies to positively identify diseased tissue before anatomical changes are visible. The goal of molecular imaging is to visualize the dynamics of disease development and cellular phenotype change, the local inflammatory response, the distribution and activity of drugs, and heterogeneities in otherwise anatomically invisible pathological tissue. Many medical imaging techniques including optical imaging,[3] magnetic resonance imaging (MRI),[4] optical coherence tomography (OCT),[5] ultrasound imaging,[6,7] positron emission tomography (PET),[8] single-photon emission computed tomography (SPECT),[9] and recently photoacoustic (PA) imaging[10] have developed strategies for molecular imaging. These techniques have specific molecular contrast agents, such as radioactive isotopes for PET/SPECT,[9] infrared and cyanine dyes for optical imaging,[11] gadolinium solutions and iron-oxide nanoparticles (NPs) for MRI,[12] and microbubbles for ultrasound imaging.[13] The accumulation of molecular markers in the targeted tissue can be imaged to provide information at the resolution of the technique, but it is often quite difficult to quantify the local amount of the marker. Clinically, such a quantification process is typically performed *ex vivo* by mass spectrometry. Although mass spectrometry provides accurate quantitation, the spatial distribution of the markers is lost.[14] Therefore, a reliable tool to relate *in vivo* molecular images of pathological tissue to spatially resolved quantitative maps of the presence of recognition markers is highly desirable.

Photoacoustic imaging is a relatively new medical imaging modality that formulates images based on the local optical absorption. In PA imaging, hemoglobin of different oxygenation states and fat deposition are typical endogenous contrast sources.[15,16] Furthermore, PA imaging can utilize exogenous contrast agents such as dyes, carbon nanotubes, or plasmonic NPs.[17] Photoacoustic imaging can be implemented as a tomographic technique[18−20] or as a

* Address correspondence to emelian@mail.utexas.edu.

Received for review October 12, 2012 and accepted January 11, 2013.

Published online January 11, 2013
10.1021/nn304739s

microscopy technique,[21−23] which promises to study and quantify the local distribution of endogenous and exogenous absorbers. For instance, PA microscopy can provide functional information by imaging the local blood oxygenation[21] by correlating the optical absorption spectra of oxygenated and deoxygenated hemoglobin to the spectroscopic PA signal. Photoacoustic microscopes have also been used for pathological imaging of melanoma[20] and amyloid plaques.[23] Unlike optical microscopy techniques (confocal, bright-field, and dark-field microscopy), where generally both the optical absorption and scattering contribute to the signal, the signal in PA microscopy is based solely on the optical absorption because it is acoustic waves, which have longer wavelengths, that are being detected. Since optical scattering is typically the dominant mechanism of interaction with cells and tissues,[24] PA images often have higher contrast and specificity than the optical techniques.

Nanoparticle-augmented PA imaging is a new branch of PA imaging that derives its contrast from NPs with a very high optical absorption at desired visible or near-infrared optical wavelengths. The introduction of a stable, inexpensive, and nonionizing contrast agent with targeting functionality enables molecular PA imaging to provide functional and pathological information at high resolution.[10,25−29] The highly localized labeling and label stability permit quantitative and longitudinal studies, which can be implemented as a microscopy technique with cellular and subcellular resolution.[30] Nanoparticle-augmented PA imaging is particularly suited for quantifying the local accumulation of NP markers, because the mechanism of PA signal generation is different from that of homogeneous absorbers. While the absorber is the NP, the signal is generated by the surrounding fluid and heat transfer dominates the signal generation process.[31] Therefore, the signal is proportional to the energy deposited into each NP and the thermoacoustic properties of the environment.

Most forms of PA microscopy utilize focused optical illumination for the PA signal generation and an ultrasound transducer for PA signal acquisition. For optically transparent or thin samples, the spatial resolution is determined by the optical focus within a penetration depth of one mean free path, while light scattering diminishes the resolution for larger depths. For instance, a confocal laser-scanning PA microscope recently achieved a resolution of 0.5 μm using gold nanorods for contrast, but with very high fluences to achieve measurable PA signals.[30] Even if the focal spot size does not change significantly, the local fluence will be different at the absorber in a scattering medium. Any PA microscopy method to quantify the local number of particles will therefore have to be independent of the local fluence.

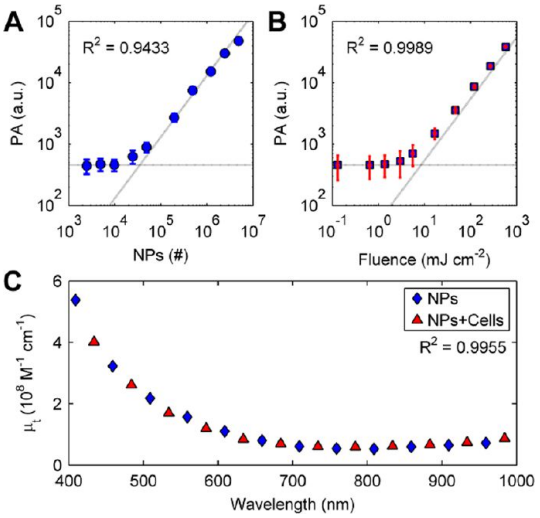

Figure 1. Dependence of PA signal on the NP quantity and laser fluence. The average PA signal *versus* (a) NP quantity and (b) laser fluence. The error bars indicate one standard deviation for each measure. The diagonal line is a linear least-squares regression with forced intercept of zero of the data above the detection threshold, and the corresponding equation and coefficient of determination (R^2) shown in the upper left corner of the plot. The horizontal lines indicate the detection threshold. (c) Molar extinction coefficient for NPs in water and NPs in cells measured as a function of optical wavelength.

We introduce a systematic approach for quantitative PA (qPA) imaging of NP markers in cell and tissue samples. Quantitative PA imaging is based on the linearity of the PA signal, P_{max}, the number of NPs, N_{NP}, with a wavelength-dependent optical absorption cross-section, $\sigma(\lambda)$, in the illuminated volume with fluence, F, and the energy that is deposited (σF). This relationship is given as:

$$P_{max}(F) - P_0(F) \propto \Gamma_{eff}\sigma(\lambda)N_{NP}F \quad (1)$$

where Γ_{eff} is the effective Grüneisen coefficient for a given NP in a nonabsorbing solvent and P_0 is the PA signal from any endogenous absorbers. This relationship holds as long as the irradiated volume is small compared to the detected acoustic wavelength, the NP absorption cross-section and environment are constant, and particle-to-particle thermal and electromagnetic coupling can be neglected. If P_0 is negligible, then P_{max} results from the NPs only and $\sigma\Gamma_{eff}$ is a constant that can be measured independently. This simple relationship makes it possible to calibrate the PA signal for a fixed fluence as a function of a known NP quantity or for a fixed known NP quantity as a function of fluence.

Since the optical scattering effects cannot be ignored in tissues, we modified eq 1 from being a function of known fluence to being a function of the relative change in fluence. This eliminates the need for sophisticated models or methods to determine the local fluence and also provides a means to validate, in each qPA imaging sample, the necessary linearity needed

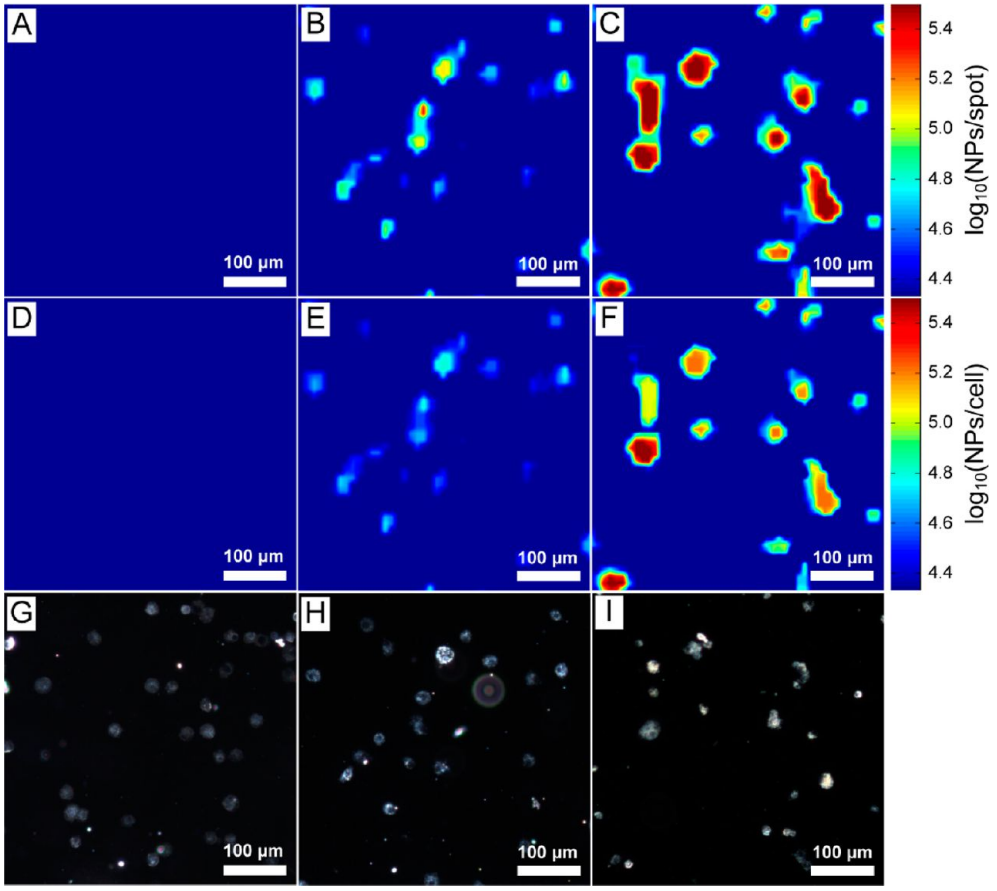

Figure 2. Quantitative PA imaging results (a–f) and co-registered dark-field microscopy (g–i) of J774A.1 cells incubated with and without NPs. Quantitative PA images scaled to the number of NPs per focal spot (a–c) and number of NPs per cell (d–f) are shown. Images of cells incubated without NPs (a, d, and g), with 1.9×10^{12} NPs per mL of cell culture media (b, e, h), and with 3.7×10^{12} NPs per mL of cell culture media (c, f, i) are shown.

for quantitation. These benefits make qPA imaging a very robust quantitation technique.

In this article we demonstrated qPA imaging of cells and thin tissue sections using a custom PA microscope. A calibration procedure to find $\sigma\Gamma_{\text{eff}}$, and thus enabling qPA, for 15 nm iron-oxide spheres dispersed in standard histology mounting media is shown. Quantitative PA imaging was used to quantify the number of NPs per cell, and the quantitation accuracy was verified using inductively coupled plasma mass spectrometry (ICP-MS). We then applied the modified qPA calibration to thin tissue slices of a NP-laden xenograft epithelial tumor.

RESULTS AND DISCUSSION

To quantitatively image NPs in cells and thin tissue slices, we built a custom PA microscope optimized for high sensitivity, while maintaining good spatial resolution. Typical PA microscopes are designed to provide high-resolution images; however, there is a balance between the spatial resolution and the ability to quantify the amount of absorber at any given point in the image, as the signal depends on the number of particles within one focal spot. High-resolution PA microscopes can increase their PA signal using high fluences (see eq 1), but at the risk of potential damage to the cells, tissues, and NPs. We produced a focal spot size (1.5×10^{-5} cm^2 at a wavelength of 532 nm) that would allow for sufficient PA signal over a wide range of fluences. To demonstrate the principles of qPA imaging, nonplasmonic iron-oxide nanoparticles were used to ensure no particle-to-particle thermal and electromagnetic coupling. Unlike plasmonic nanospheres or nanorods that can plasmon couple at high density, iron-oxide NPs have linear absorption with fluence. The surrounding media was standard histology mounting solution with unknown mechanical and thermal properties. The samples were placed between a glass microscope slide and glass coverslip with thicknesses of less than 25 μm to achieve optical focus-based resolution in a nonconfocal setting. The onset of a measurable background signal from the surrounding medium, which would be fluence dependent, was estimated in the mounting media to be greater than 2000 mJ/cm^2. However, visible damage in tissue samples occurred above ~650 mJ/cm^2.

The linear relationship between the PA signal and the number of NPs in the illuminated volume, *i.e.*, the

image pixel, was verified by a set of 10 histology phantoms with varying NP concentration, using a laser fluence of 360 mJ/cm^2. The sample thickness of 25 μm still allows for an exact conversion of the concentration to the number of NPs. The PA intensity demonstrated the expected linear dependence with NP quantity once the signal had risen above the system's detection threshold (Figure 1a). The slope, together with the fluence used, gives the proportionality factor $\sigma\Gamma_{eff}$ from eq 1 as 3.47×10^{-5}. The minimum number of NPs that could be detected at this fluence was approximately 2×10^4 NPs in a volume of 8 fL, or about 4 μM; an increase in fluence would only slightly improve this detection threshold, because damage would occur at approximately twice this fluence.

Using a phantom with 2×10^7 NPs per spot, the linear PA signal dependence with laser fluence was also confirmed (Figure 1b). In this case the slope of the line was equal to $\sigma\Gamma_{eff}N$, again resulting in a $\sigma\Gamma_{eff}$ of 3.47×10^{-5}, as expected. Additionally, the absorption spectrum of the NPs does not change when the NPs are dispersed in solution or aggregated in cells, ensuring that only quantity and laser fluence will impact the PA signal (Figure 1c).

The above calibration to determine the proportionality factor $\sigma\Gamma_{eff}$ was performed immediately before each of the following experiments to avoid setup variations. To validate quantitation, qPA images of J774A.1 murine macrophages loaded with NPs were compared to ICP-MS. Quantitative PA images were collected for cells incubated with 0, 1.9×10^{12}, and 3.7×10^{12} NPs per mL seeded at low cell density (600 cells per mm^2). A subarea of the overall qPA images is shown in Figure 2 along with co-registered dark-field microscopy images. Although visible in the dark-field microscopy images (Figure 2g), cells that were not incubated with NPs resulted in baseline level PA signals corresponding to no NPs per cell (Figure 2d). Cells incubated with NPs showed a clear PA signal indicative of NP uptake (Figure 2e and f), and the PA images are co-registered with their respective dark-field images (Figure 2h and i). Quantitative PA imaging of ~1000 cells (based on the dark-field image cell counts) measured averages of 6.29×10^4 and 1.06×10^5 NPs per cell for the incubation concentrations of 1.9×10^{12} and 3.7×10^{12} NPs per mL, respectively. The cell-to-cell standard deviations for each respective sample were 2.37×10^4 and 5.24×10^4. The blurring between cells in Figure 2e and f results from the focal spot size being larger than the cells.

The qPA averages correlate well with the ICP-MS results of 6.32×10^4 and 1.08×10^5 NPs per cell (ICP-MS standard deviations were 0.029×10^4 and 0.027×10^5, respectively). The averages from both cell samples had negative deviations that were likely due to the sensitivity of the PA microscope to iron-oxide NPs: the minimum number of NPs that could be detected

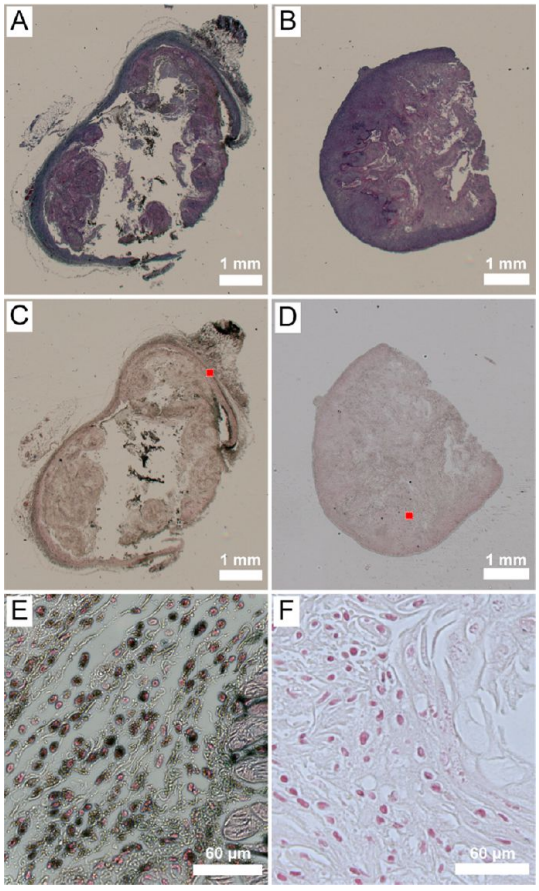

Figure 3. Bright-field optical microscopy images at 1.25× of tumor slices with H&E stain (a, b) and Prussian blue stain with nuclear fast red counterstain (c, d). The tumor from the mouse inoculated with NPs is shown in images (a), (c), and (e). The tumor from the mouse with no NP inoculation is shown in (b), (d), and (f). The 40× magnification images (e, f) correspond to regions marked in (c) and (d), respectively.

was 2×10^4. To overcome this sensitivity, we repeated the qPA experiment with cells seeded at high density (7×10^4 cells per mm^2) for a total of 5×10^5 cells. Again, the cells with no incubation of NPs resulted in 0 NPs per mL in the qPA images. Quantitative PA analysis measured averages of 6.44×10^4 and 1.17×10^5 NPs per cell, with cell-to-cell standard deviations of 1.12×10^4 and 0.31×10^5, respectively. The qPA image analysis therefore leads to an accurate determination of the number of NPs per cell with errors of well below 10%.

While for individual cells the direct calibration is sufficient to accurately determine the local number of NPs, tissue samples can provide environments where the simple linear relationship is no longer fulfilled.[31] Additionally, in more complex samples the local fluence could be lower than the fluence used in the calibration due to optical scattering. However, the PA signal constant $\sigma\Gamma_{eff}$ does not change, as long as conditions for the local environment and noninteracting NPs are fulfilled, and can be determined by an external calibration against the NP number as before. Then, the local number of NPs for any fluence attenuation

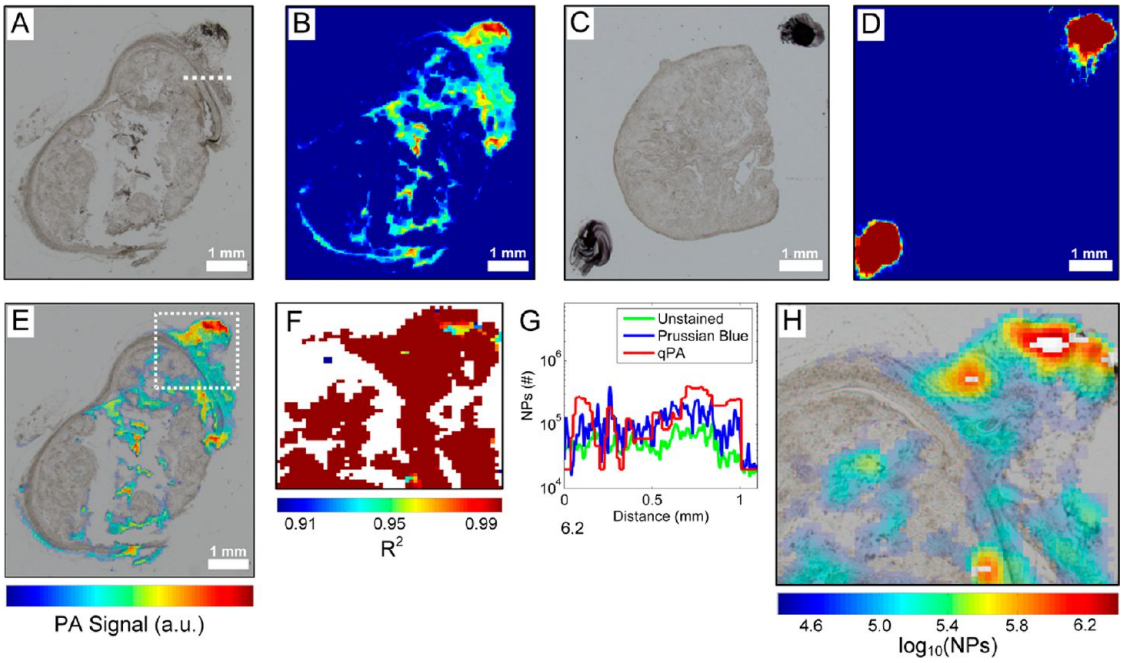

Figure 4. Bright-field microscopy (a and c) and PA (b and d) images of unstained tumor slices with (a and b) and without (c and d) NPs. An overlay of the optical and PA image of the tumor with NPs from (a) and (b) are shown in (e). R^2 map of the area in the white box in (e) is shown in (f). Quantitative PA image using $R^2 > 0.97$ with unquantifiable areas in white is shown in (h). (g) Quantitative comparison of the unstained and Prussian blue stained bright-field images and the qPA images. The values for the graphs were generated from a line shown in (a).

α can be determined by the slope of the PA pressure *versus* fluence with $P_0 \approx 0$:

$$\alpha P_{max}(F) \propto \Gamma_{eff}\sigma N_{NP}\alpha F \quad (2)$$

and

$$N_{NP} = \frac{\alpha(P_{max}(F_2) - P_{max}(F_1))}{\alpha(F_2 - F_1)}(\Gamma_{eff}\sigma)^{-1} \quad (3)$$

Mapping the PA signal with at least two fluences (F_1 and F_2 in eq 3) above the detection threshold of the system, with an intercept at the origin, allows for the accurate determination of the local NP quantity by assessing the attenuated changes in the PA signal with the changes in attenuated fluence. Therefore, there is no need for extraneous approaches to determine the local fluence in turbid media, such as tissue. This technique also excludes pixels that do not show a linear dependence due to thermal damage or thermal coupling, further adding robustness to the qPA technique.

The quantitative molecular imaging capability was demonstrated in histological slices of a xenograft A431 human epithelial carcinoma with injected NPs. Sections from an A431 carcinoma were hematoxylin and eosin (H&E) stained and show typical tumor morphology (Figure 3a and b), while Prussian blue staining indicates the presence of iron (Figure 3c and d). High-magnification (40×) images of Prussian blue-stained samples show cellular uptake of the NPs (Figure 3e), in comparison to the NP-free control (Figure 3f). For the qPA microscopy of slices of the tumor with and without NPs, unstained histology sections directly adjacent to the respective stained slices (Figure 4b and d) were used, and the PA maps are shown in Figure 4c and e, respectively. Black ink marks on the glass coverslip were used for registration of the PA image with the bright-field optical microscopy images because black ink is a high-contrast source in both imaging techniques.

The tumor slice with no NP inoculation (Figure 4c) produced only system noise level PA signals independent of fluence, indicating the absence of NPs (Figure 4d). In contrast, the tumor inoculated with NPs (Figure 4a) clearly showed a distribution of PA signal levels (Figure 4b), which for the higher levels of signal clearly co-registered with the stained areas in Figure 3c.

To quantify the local NPs, four fluences were chosen between 50 and 360 mJ/cm^2, and a subsection of the sample (as outlined in Figure 4e) was scanned at each fluence. For each pixel a line through the origin (no signal at zero fluence) was fitted through the PA signals above the noise floor of the system as a function of fluence. The quality of the fit (R^2) for each image pixel as determined from the slope of the fit for regressions above 0.9 is shown in Figure 4f, where pixels that produced only background were left blank. Pixels with an $R^2 < 0.97$ were not quantified due to a lack of confidence, and in the cases where the linear fluence dependence was not strong ($R^2 < 0.97$), the high-fluence PA signals were not included in the quantification procedure in attempts to eliminate nonlinearities corresponding to interacting particles or damaging heat. The resulting map is a quantified image of the

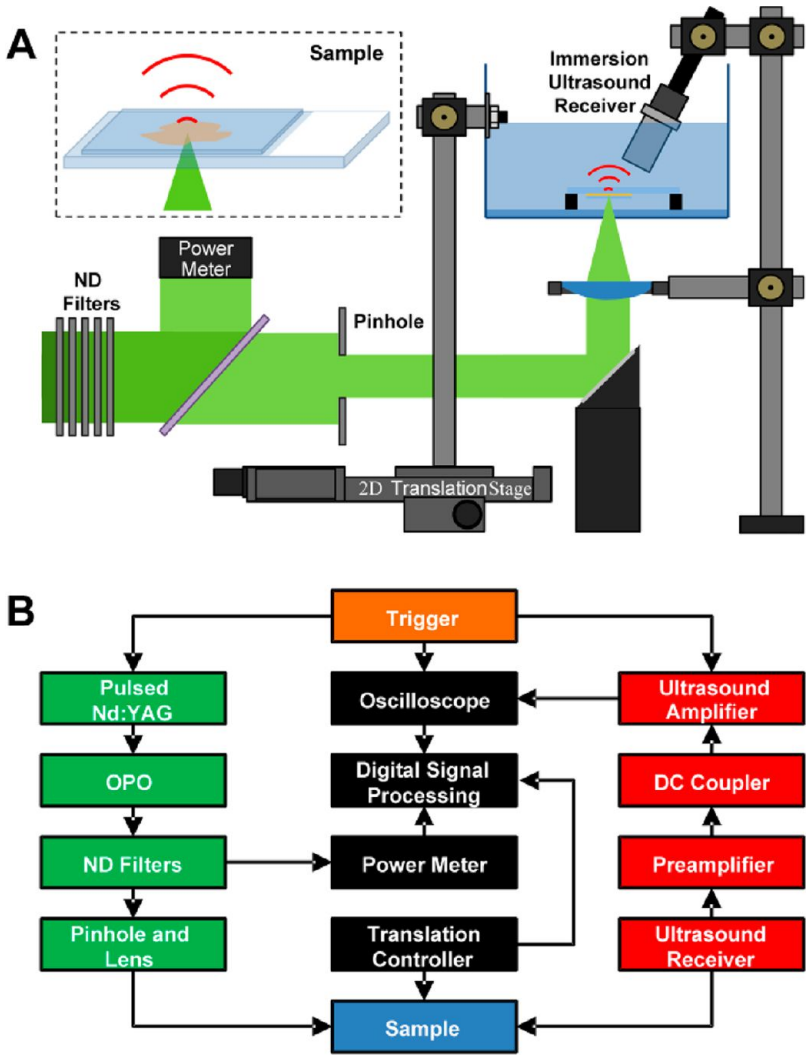

Figure 5. Drawing (a) and schematic diagram (b) of the PA microscope to quantitatively image NPs in histology.

NP number distribution (Figure 4h) that was determined with high confidence.

Comparing the quantified maps (Figure 4h) to the nonquantified PA maps (Figure 4b), most of the pixels with PA signals could be quantified (Figure 4f). Some low-signal regions were not quantified due to the choice of the four fluences. Areas of very high signals—and very strong Prussian blue staining in Figure 3c—could not be quantified because nonlinear effects dominate the high-fluence signals. Additionally, the qPA-determined NP quantities in the trusted pixels were very close to those simply based on a single-fluence calibration, indicating a very low scattering environment. Comparing the qPA images to Prussian blue stained images (Figure 3c), many areas positively identified NPs at locations that would not have had a clear staining in standard histology, at least at lower magnifications. A more detailed analysis comparing the qPA image to the bright-field microscopy images of the unstained and Prussian blue stained histology is shown in Figure 4g. The gray scale intensities along a

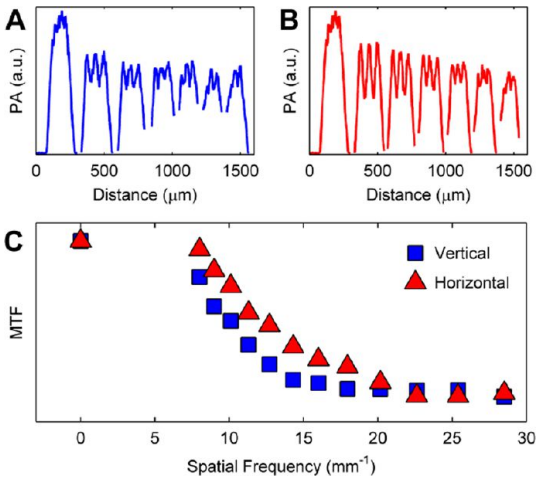

Figure 6. Characterization of the resolution of the PA microscope using a USAF 1951 positive resolution target with step size of 2 μm by 2 μm. PA intensity *versus* distance for spatial frequencies ~0 and 16−28.5 mm^{-1} along the (a) vertical axis and (b) horizontal axis. (c) MTF *versus* spatial frequency indicating an elliptical focal spot with axis diameters of 39.4 μm (horizontal) by 49.6 μm (vertical).

line in the Prussian blue image were scaled to match the overall range of the corresponding qPA image. Then, the same line in the unstained histology (Figure 4a) was scaled using the same factor used in the analysis of the Prussian blue image. The comparison of the Prussian blue, unstained histology, and qPA curves presented in Figure 4g demonstrates superior sensitivity and specificity of qPA for the NPs in comparison to both optical imaging techniques, as optical scattering dominates the bright-field images. Therefore, qPA microscopy has not only higher NP contrast than the typical histology detection, which requires an additional labeling step, but also a lower detection limit, at least at lower magnifications. Quantitative PA microscopy is well suited to validate *in vivo* PA imaging because it combines both the quantitation (typically provided by mass spectrometry) and the NP distribution (typically provided by histological staining).

CONCLUSIONS

We developed a qPA microscope including a method to reliably quantify the number of absorbers, such as iron-oxide NPs, delivered to cells and tissues of interest. The method is based on the linearity of the PA signal with both local NP quantity and local fluence, but it does not depend on the knowledge of the local fluence. Accurate quantization was achieved using a qPA microscope with a detection limit of $\sim 2 \times 10^4$ NPs per focal spot. The qPA image of the NP-laden, *ex vivo* tissue slice was in good agreement with traditional histopathological analysis, but with higher sensitivity. Overall, we demonstrated that qPA imaging is an accurate quantitation technique and can be used to determine the efficiency and effectiveness of molecular targeting strategies in both *in vitro* cell studies and *ex vivo* tissue samples. Since the spatial distribution is preserved in the quantitation, qPA imaging can also validate *in vivo* molecular imaging results.

Although iron-oxide NPs were used in our study, other types of NPs that do not plasmon couple can be used (including, but not limited to, gadolinium oxide, manganese oxide, doped iron oxides, and silica-coated gold NPs). To quantify plasmonic NPs, the developed approach may need to include spectroscopic PA imaging techniques because of the spectral changes in the optical absorption resulting from surface plasmon coupling. The detection limit can be significantly improved by signal-to-noise improvements in the microscope and by the use of NPs that produce an increased PA signal, such as thermally stable and electromagnetically isolated plasmonic NPs. Although the methods developed here are applied to the microscopy of thin samples, qPA imaging can be used to provide quantitative maps for thick samples, including *in vivo* tissues, by incorporating spectroscopic techniques to uncouple the contributions of the NPs from the endogenous absorbers and by varying laser pulse-widths to eliminate the effects of constructive and destructive acoustic interference. Quantitative PA imaging not only can provide essential information to progress medical imaging technology but also has the potential to be a stand-alone technique to improve diagnostics and prognostics of disease.

METHODS

A custom PA microscope was developed to quantify molecular sensing NPs in cell and tissue samples. A drawing and schematic diagram of the PA microscope are shown in Figure 5. The PA excitation was generated by a Q-switched, pulsed Nd:YAG laser (Quanta-Ray PRO-290, Spectra-Physics Lasers, Mountain View, CA, USA) pumping a tunable optical panametric oscillator (OPO) (Spectra-Physics premiScan/MB, GWU-Lasertechnik Vertriebsges, Germany). The laser output, with a wavelength of 532 nm, had a pulse-width of 5−7 ns and a pulse repetition rate of 10 Hz. The laser energy from the oscillator was controlled by an array of neutral density (ND) filters, and a 5 mm aperture was used to reject beam irregularity. The laser beam was then split with one beam used for measuring the laser energy with a pyroelectric power meter (Nova II, Ophir Ltd., Jerusalem, Israel), and the other beam was focused on the sample using a plano-convex lens (LA1401, Thorlabs Inc., Newton, NJ, USA) with a focal length of 60 mm and a diameter of 50.8 mm. All fluences were compensated for pulse-to-pulse fluctuations in the laser energy.

Water was used as an acoustic coupling medium to reduce the acoustic impedance between the sample and the ultrasound receiver. The converging laser beam from the plano-convex lens was transmitted through a 1 mm glass microscope slide (optical window for the water tank), 5 mm of water, and a 1 mm glass microscope slide before focusing on the phantom/cell/tissue sample (dashed box in Figure 5a). The induced PA pressure wave propagated through the 0.2 mm thick glass coverslip and 25 mm of water before being measured by a 1 mm needle hydrophone with 4 dB bandwidth of 0.2−15 MHz (Precision Acoustics LTD, Dorchester, UK). The PA signal acquired by the hydrophone was amplified by an ultrasound receive amplifier (5073PR, Olympus NDT Inc., Waltham, MA, USA) with a gain of 39 dB. The amplified PA signal was digitized using an oscilloscope (CompuScope 12400, Gage Applied Technologies Inc., Lockport, IL, USA) with sampling frequency of 200 MHz.

Triggering of the pulsed laser system, the ultrasound receive electronics, and the movement of a two-axis translation stage (T-XY-LSM100A-KT02, Zaber Technologies Inc., Vancouver, Canada), to raster-scan the sample while the optical and ultrasound systems remained stationary, was coordinated by custom software. A 20 μm by 25 μm step size was used for the cell and the tissue samples. Four spatially registered and energy-compensated PA A-lines from each position of the scan were postprocessed using a band-pass filter to remove electronic noise outside of the bandwidth of the hydrophone. The four A-lines were then averaged, and the maximum signal was used for the PA signal.

PA Microscope Characterization. The spot size was characterized with a USAF 1951 positive resolution target (DA009, Max Levy Autograph, Inc., Philadelphia, PA, USA) to determine the illuminated volume in the sample to enable accurate quantitation of $\sigma\Gamma_{\text{eff}}$. The laser beam was focused by adjusting the plano-convex lens to produce the maximum PA signal in the resolution target. Using a step size of 2 μm by 2 μm for spatial frequencies varying from $\sim$0 to 30 mm^{-1} and laser energy of $\sim$1 μJ, a PA image of the resolution target was produced

(linear scans are shown in Figure 6a and b). To determine the focal spot size, the modulation transfer function (MTF) was calculated for each spatial frequency. The MFT is defined as

$$\text{MTF} = \frac{M_{\text{element}}}{M_{\text{ideal}}}, \quad M = \frac{I_{\max} - I_{\min}}{I_{\max} + I_{\min}} \tag{4}$$

where M_{element} is the modulation of the element, M_{ideal} is the modulation of the element 0 and background signal from the background of the slide, $I_{\max}$ is the maximum PA intensity, and $I_{\min}$ is the minimum PA intensity. A 0.15 cutoff MTF was calculated in a large element of the resolution target.

After analyzing the MTF (Figure 6c), a focal spot size of 39 μm horizontal by 50 μm vertical was determined; the elliptic shape most likely results from the anisotropic beam divergence from the nonlinear optical crystal in the OPO. The focal spot size was confirmed by scanning the step function of one of the large elements in the resolution target with a 25% PA signal cutoff. Therefore, the probing volume is $\sim 8 \times 10^{-12}$ $L = 8$ fL for the histology samples with a 5 μm sample thickness. This resolution, while limiting the imaging to small cell groups, has the benefit of illuminating a sufficient amount of NPs for a measurable PA signal, while maintaining fluences low enough not to cause excessive heating, large background signals, and irreversible changes.

For all experiments 15 nm Fe_3O_4 spheres were used; they were synthesized using a one-pot thermal decomposition method.[32] The NP size was characterized using a DelsaNano C particle analyzer (Beckman Coulter Inc., Indianapolis, IN, USA). The NPs were then stabilized with dextran in water by *in situ* co-precipitation from an iron salt−dextran solution.[33] The NPs were then centrifuged, and the supernatant was removed, resuspended in Shandon* ClearVue Mount (Thermo Scientific LLC, Waltham, MA, USA), and sonicated for one hour. To correlate the number of NPs with the PA signal, phantoms were constructed with varying concentrations of NPs. A volume of 25 μL of NP solution was placed on a 1 mm thick microscope glass slide. A 25 μm stainless steel spacer (McMaster Carr Supply Company, Elmhurst, IL, USA) was placed on the slide to standardize the sample thickness. The sample was then covered by a 50 μm glass coverslip and remained at room temperature for 6 h before being sealed with fingernail polish. A laser energy of 5.6 μJ was used to measure the PA signal dependence with the NP quantity, and a phantom with 5.2×10^{14} NPs per mL was used for the laser fluence dependence. For each phantom experiment, 200 laser-induced PA signals at 10 different positions were averaged. All correlation studies were repeated four times and additionally repeated before every imaging measurement to avoid apparatus variations.

Cell Study. *In vitro* murine J774A.1 macrophage cells were cultured using phenol-free DMEM/F12 (Life Technologies Corp., Grand Island, NY, USA) cell medium supplemented with 10% fetal bovine serum (Phenix Research Products Inc., Candler, NC, USA). After the cells reached ~70% confluence, adherent cells were incubated with 1.9×10^{12} NPs and 3.7×10^{12} NPs per mL of cell culture media, respectively. After 22 h the cells were rinsed with phosphate-buffered saline three times, removed from the cell culture flasks, and fixed in 10% formalin. After 2 h, the cells were centrifuged to remove excess formalin and resuspended in deionized water. Aliquots of 20 μL of the cell suspension were placed on microscope slides, dried at 60 °C, mounted with Shandon* ClearVue Mount, and sealed in a coverslip. These samples had an average of 5×10^5 cells per slide and were used to determine the average number of NPs per cell using the PA microscope. These samples included a small 25 μm thick stainless steel marker placed between the microscope slide and coverslip for dark-field optical image co-registration (DMI 3000 B, Leica Microsystems GmbH, Germany).

The molar extinction of cell suspensions in water was analyzed using a spectrophotometer (UV-3600, Shimadzu Corp. Kyoto, Japan). Spectra from known concentrations of NPs were acquired and used to determine the molar extinction coefficient. The number of NPs in cells incubated with 3.7×10^{12} NPs per mL of media was quantified using ICP-MS, and then extinction spectra were acquired. Cells without NPs were used to subtract the contribution of the cells to the molar extinction coefficient of the NPs.

Quantitative PA imaging results were compared to a quadrupole ICP-MS (Agilent 7500ce, Agilent Technologies Inc., Santa Clara, CA, USA) with H_2 as the reaction gas. Samples of 1×10^7 cells incubated with 0, 7.5×10^{12}, and 1.9×10^{13} NPs per mL of cell culture media were each placed in polyethylene containers, dehydrated at 60 °C, dissolved in 70% HNO_3 for 24 h at 60 °C, and diluted to a final concentration of 2% HNO_3. Estimating an average of 71700 iron atoms per NP, the ICP-MS results were converted to number of NPs per cell.

Animal Model. Xenograft A431 human epithelial carcinoma tumors were grown in the flank of a Nu/Nu mouse. First, A431 carcinoma cells were cultured *in vitro* using phenol-free DMEM/F12 cell medium supplemented with 10% fetal bovine serum. The cells (2.4×10^6) were then suspended in 400 μL of phosphate-buffered saline and injected into the right flanks of two mice, 200 μL in each mouse. After 2 weeks when the tumors reached 8−10 mm in diameter, approximately 5×10^{13} NPs were directly injected into the tumor of one mouse. The other mouse served as a control for the study. During all injections, the mice were anesthetized with avertin. One day after the NP inoculation, both mice were euthanized by carbon dioxide asphyxiation followed by cerebral dislocation, and the tumors were harvested for histology. All experimental animal procedures were performed in compliance with the National Institutes of Health, and the animal protocol was approved by the University of Texas at Austin Institutional Animal Care and Use Committee.

Histology. The harvested tumors were placed in 10% neutral buffered formalin for 24 h for fixation of the tissue. The tumors were then transferred into a solution of 70% ethanol and sent to the University of Texas M.D. Anderson Cancer Center Science Park, Department of Molecular Carcinogenesis (Smithville, TX 78957, USA), for histology preparation. The tumors were placed into a Shandon* Excelsior tissue processor (Thermo Scientific LLC) to be dehydrated by increasing the ethanol content from 70% to 100%, cleared with Shandon* Xylene Substitute (Thermo Scientific LLC), and infiltrated with Paraplast (McCormick Scientific LLC, Richmond, IL, USA). The tumors were then embedded into Paraplast mold, sliced into 5 μm thick sections, and placed on 1 mm thick glass microscope slides.

The unstained slides were then deparaffinized by heating the slides to 60 °C for 30 min, cooled to room temperature, soaked in xylene substitute for 10 min, soaked in 100% ethanol for 10 min, and rinsed with deionized water (diH_2O). Hematoxylin and eosin stained slides were processed in a Shandon* Varistain Gemini Slide Stainer (Thermo Scientific LLC) by first deparaffinizing the sample and staining with Shandon* Gill 2 Hematoxylin (Thermo Scientific LLC) and Shandon* Eosin Y (Thermo Scientific LLC) for 4 min. The stained samples were then rinsed with diH_2O and dehydrated. Prussian blue stain was used to visualize the presence of NPs in the tissues by staining the iron atoms and was processed by deparaffinizing the samples and placing the samples in equal parts 2% potassium ferrocyanide (Sigma-Aldrich Corp., St. Louis, MO, USA) and 2% hydrochloric acid. The solution and sample were then heated for 20 min at 60 °C. The stained samples were then rinsed in diH_2O and counterstained in nuclear-fast red (American Master Tech Scientific Inc., Lodi, CA, USA) for 5 min. The samples were rinsed again in diH_2O and dehydrated. After staining, the samples were dehydrated using ethanol and xylene substitute. The tissue was then coated with Shandon* ClearVue Mount mounting media and sealed with a 50 μm thick glass coverslip.

The unstained, H&E stained, and Prussian blue stained histology samples were first bright-field imaged using the aforementioned optical microscope with a 1.25× objective. Black marks using a marker (14-905-30, Fisherbrand Securline Marker II pens, Fisher Scientific Company LLC, Pittsburgh, PA, USA) were place on the coverslip of the unstained histology sample for image co-registration with the PA image, and the slide was reimaged using the 1.25× objective. Using a 40× objective, the Prussian blue histology sample was bright-field imaged to confirm NP delivery into the tissue.

Conflict of Interest: The authors declare no competing financial interest.

Acknowledgment. We thank Mohammad Mehrmohammadi from the University of Texas at Austin for his help with the animal procedures, Yun-Sheng Chen from the University of Texas at Austin for his help with some of the theoretical aspects of this project, and Dr. Nathan Miller in the Quadrupole ICP-MS Lab at the University of Texas at Austin for the ICP-MS analysis. This work was partially supported by the National Institutes of Health under grants CA 149740 and EB 008101.

REFERENCES AND NOTES

1. Weissleder, R.; Mahmood, U. Molecular Imaging. *Radiology* **2001**, *219*, 316–333.
2. Massoud, T. F.; Gambhir, S. S. Molecular Imaging in Living Subjects: Seeing Fundamental Biological Processes in a New Light. *Genes Dev.* **2003**, *17*, 545–580.
3. Bremer, C.; Ntziachristos, V.; Weissleder, R. Optical-Based Molecular Imaging: Contrast Agents and Potential Medical Applications. *Eur. Radiol.* **2003**, *13*, 231–243.
4. Aime, S.; Castelli, D. D.; Crich, S. G.; Gianolio, E.; Terreno, E. Pushing the Sensitivity Envelope of Lanthanide-Based Magnetic Resonance Imaging (MRI) Contrast Agents for Molecular Imaging Applications. *Acc. Chem. Res.* **2009**, *42*, 822–831.
5. Rao, K. D.; Choma, M. A.; Yazdanfar, S.; Rollins, A. M.; Izatt, J. A. Molecular Contrast in Optical Coherence Tomography by Use of a Pump Probe Technique. *Opt. Lett.* **2003**, *28*, 340–342.
6. Kaufmann, B. A.; Sanders, J. M.; Davis, C.; Xie, A.; Aldred, P.; Sarembock, I. J.; Lindner, J. R. Molecular Imaging of Inflammation in Atherosclerosis with Targeted Ultrasound Detection of Vascular Cell Adhesion Molecule-1. *Circulation* **2007**, *116*, 276–284.
7. Kaufmann, B. A.; Lindner, J. R. Molecular Imaging with Targeted Contrast Ultrasound. *Curr. Opin. Biotechnol.* **2007**, *18*, 11–16.
8. Gambhir, S. S. Molecular Imaging of Cancer with Positron Emission Tomography. *Nat. Rev. Cancer* **2002**, *2*, 683–693.
9. Sharma, V.; Luker, G. D.; Piwnica-Worms, D. Molecular Imaging of Gene Expression and Protein Function *in Vivo* with PET and SPECT. *J. Magn. Reson. Imaging* **2002**, *16*, 336–351.
10. Mallidi, S.; Larson, T.; Tam, J.; Joshi, P. P.; Karpiouk, A.; Sokolov, K.; Emelianov, S. Multiwavelength Photoacoustic Imaging and Plasmon Resonance Coupling of Gold Nanoparticles for Selective Detection of Cancer. *Nano Lett.* **2009**, *9*, 2825–2831.
11. Choy, G.; Choyke, P.; Libutti, S. K. Current Advances in Molecular Imaging: Noninvasive *in Vivo* Bioluminescent and Fluorescent Optical Imaging in Cancer Research. *Mol. Imaging* **2003**, *2*, 303–312.
12. Artemov, D.; Mori, N.; Okollie, B.; Bhujwalla, Z. M. MR Molecular Imaging of the Her-2/neu Receptor in Breast Cancer Cells Using Targeted Iron Oxide Nanoparticles. *Magn. Reson. Med.* **2003**, *49*, 403–408.
13. Lindner, J. R. Molecular Imaging with Contrast Ultrasound and Targeted Microbubbles. *J. Nucl. Cardiol.* **2004**, *11*, 215–221.
14. Qian, X.; Peng, X. H.; Ansari, D. O.; Yin-Goen, Q.; Chen, G. Z.; Shin, D. M.; Yang, L.; Young, A. N.; Wang, M. D.; Nie, S. *In Vivo* Tumor Targeting and Spectroscopic Detection with Surface-Enhanced Raman Nanoparticle Tags. *Nat. Biotechnol.* **2007**, *26*, 83–90.
15. Wang, B.; Emelianov, S. Thermal Intravascular Photoacoustic Imaging. *Biomed. Opt. Express* **2011**, *2*, 3072–3078.
16. Kim, S.; Chen, Y. S.; Luke, G. P.; Emelianov, S. Y. *In Vivo* Three-Dimensional Spectroscopic Photoacoustic Imaging for Monitoring Nanoparticle Delivery. *Biomed. Opt. Express* **2011**, *2*, 2540–2550.
17. Luke, G. P.; Yeager, D.; Emelianov, S. Y. Biomedical Applications of Photoacoustic Imaging with Exogenous Contrast Agents. *Ann. Biomed. Eng.* **2012**, *40*, 422–437.
18. Chamberland, D. L.; Agarwal, A.; Kotov, N.; Fowlkes, J. B.; Carson, P. L.; Wang, X. Photoacoustic Tomography of Joints Aided by an Etanercept-Conjugated Gold Nanoparticle Contrast Agent—an *Ex Vivo* Preliminary Rat Study. *Nanotechnology* **2008**, *19*, 095101 (7pp).
19. Copland, J. A.; Eghtedari, M.; Popov, V. L.; Kotov, N.; Mamedova, N.; Motamedi, M.; Oraevsky, A. A. Bioconjugated Gold Nanoparticles as a Molecular Based Contrast Agent: Implications for Imaging of Deep Tumors Using Optoacoustic Tomography. *Mol. Imaging Biol.* **2004**, *6*, 341–349.
20. Kim, C.; Cho, E. C.; Chen, J.; Song, K. H.; Au, L.; Favazza, C.; Zhang, Q.; Cobley, C. M.; Gao, F.; Xia, Y. *In Vivo* Molecular Photoacoustic Tomography of Melanomas Targeted by Bioconjugated Gold Nanocages. *ACS Nano* **2010**, *4*, 4559–4564.
21. Hu, S.; Maslov, K.; Wang, L. V. Noninvasive Label-Free Imaging of Microhemodynamics by Optical-Resolution Photoacoustic Microscopy. *Opt. Express* **2009**, *17*, 7688–7693.
22. Hu, S.; Maslov, K.; Wang, L. V. Second-Generation Optical-Resolution Photoacoustic Microscopy with Improved Sensitivity and Speed. *Opt. Lett.* **2011**, *36*, 1134–1136.
23. Hu, S.; Yan, P.; Maslov, K.; Lee, J. M.; Wang, L. V. Intravital Imaging of Amyloid Plaques in a Transgenic Mouse Model Using Optical-Resolution Photoacoustic Microscopy. *Opt. Lett.* **2009**, *34*, 3899–3901.
24. Cook, J. R.; Bouchard, R. R.; Emelianov, S. Y. Tissue-Mimicking Phantoms for Photoacoustic and Ultrasonic Imaging. *Biomed. Opt. Express* **2011**, *2*, 3193–3206.
25. Agarwal, A.; Huang, S.; ODonnell, M.; Day, K.; Day, M.; Kotov, N.; Ashkenazi, S. Targeted Gold Nanorod Contrast Agent for Prostate Cancer Detection by Photoacoustic Imaging. *J. Appl. Phys.* **2007**, *102*, 064701.
26. Homan, K. A.; Souza, M.; Truby, R.; Luke, G. P.; Green, C.; Vreeland, E.; Emelianov, S. Silver Nanoplate Contrast Agents for *in Vivo* Molecular Photoacoustic Imaging. *ACS Nano* **2012**, *6*, 641–650.
27. Kim, K.; Huang, S. W.; Ashkenazi, S.; ODonnell, M.; Agarwal, A.; Kotov, N. A.; Denny, M. F.; Kaplan, M. J. Photoacoustic Imaging of Early Inflammatory Response Using Gold Nanorods. *Appl. Phys. Lett.* **2007**, *90*, 223901.
28. Shah, J.; Park, S.; Aglyamov, S.; Larson, T.; Ma, L.; Sokolov, K.; Johnston, K.; Milner, T.; Emelianov, S. Y. Photoacoustic Imaging and Temperature Measurement for Photothermal Cancer Therapy. *J. Biomed. Opt.* **2008**, *13*, 034024.
29. Bao, C.; Beziere, N.; del Pino, P.; Pelaz, B.; Estrada, G.; Tian, F.; Ntziachristos, V.; de la Fuente, J. M.; Cui, D. Gold Nanoprisms as Optoacoustic Signal Nanoamplifiers for *in Vivo* Bioimaging of Gastrointestinal Cancers. *Small* **2012**, 10.1002/smll.201201779.
30. Yang, S.; Ye, F.; Xing, D. Intracellular Label-Free Gold Nanorods Imaging with Photoacoustic Microscopy. *Opt. Express* **2012**, *20*, 10370–10375.
31. Nam, S. Y.; Ricles, L. M.; Suggs, L. J.; Emelianov, S. Y. Nonlinear Photoacoustic Signal Increase of Endocytosed Gold Nanoparticles. *Opt. Lett.* **2012**, *37*, 4708–4710.
32. Gupta, A. K.; Gupta, M. Synthesis and Surface Engineering of Iron Oxide Nanoparticles for Biomedical Applications. *Biomaterials* **2005**, *26*, 3995–4021.
33. Molday, R. S.; Mackenzie, D. Immunospecific Ferromagnetic Iron-Dextran Reagents for the Labeling and Magnetic Separation of Cells. *J. Immunol. Methods* **1982**, *52*, 353–367.